Prochlorococcus phage ferredoxin: structural characterization and electron transfer to cyanobacterial sulfite reductases

Received for publication, March 18, 2020, and in revised form, May 15, 2020 Published, Papers in Press, May 19, 2020, DOI 10.1074/jbc.RA120.013501

Ian J. Campbell[1,2], Jose Luis Olmos, Jr.[1,2], Weijun Xu[2], Dimithree Kahanda[2], Joshua T. Atkinson[2], Othneil Noble Sparks[2], Mitchell D. Miller[2], George N. Phillips, Jr.[2,3], George N. Bennett[2,4], and Jonathan J. Silberg[2,4,5,*]

From the [1]Biochemistry and Cell Biology Graduate Program, Rice University, Houston, Texas, USA, [2]Department of Biosciences, Rice University, Houston, Texas, USA, [3]Department of Chemistry, Rice University, Houston, Texas, USA, [4]Department of Chemical and Biomolecular Engineering, Rice University, Houston, Texas, USA, and [5]Department of Bioengineering, Rice University, Houston, Texas, USA

Edited by Joseph M. Jez

Marine cyanobacteria are infected by phages whose genomes encode ferredoxin (Fd) electron carriers. These Fds are thought to redirect the energy harvested from light to phage-encoded oxidoreductases that enhance viral fitness, but it is unclear how the biophysical properties and partner specificities of phage Fds relate to those of photosynthetic organisms. Here, results of a bioinformatics analysis using a sequence similarity network revealed that phage Fds are most closely related to cyanobacterial Fds that transfer electrons from photosystems to oxidoreductases involved in nutrient assimilation. Structural analysis of myovirus P-SSM2 Fd (pssm2-Fd), which infects the cyanobacterium *Prochlorococcus marinus*, revealed high levels of similarity to cyanobacterial Fds (root mean square deviations of ≤0.5 Å). Additionally, pssm2-Fd exhibited a low midpoint reduction potential (−336 mV *versus* a standard hydrogen electrode), similar to other photosynthetic Fds, although it had lower thermostability (T_m = 28 °C) than did many other Fds. When expressed in an *Escherichia coli* strain deficient in sulfite assimilation, pssm2-Fd complemented bacterial growth when coexpressed with a *P. marinus* sulfite reductase, revealing that pssm2-Fd can transfer electrons to a host protein involved in nutrient assimilation. The high levels of structural similarity with cyanobacterial Fds and reactivity with a host sulfite reductase suggest that phage Fds evolved to transfer electrons to cyanobacterially encoded oxidoreductases.

Prochlorococcus marinus is thought to be the most prevalent photosynthetic organism on Earth, with a global abundance of 10^{27} cells (1), making it a key player in biogeochemical processes. This oligotrophic cyanobacterium inhabits the euphotic zone of oceans (40°N to 40°S) and is projected to expand in both density and range as global temperatures rise (1). Collectively fixing 4 gigatons of carbon annually (1), the diverse ecotypes of *P. marinus* thrive at many depths, where light, nutrient availability, and temperature vary (2–4). Up to 24% of the CO_2 fixed by *P. marinus* is released as dissolved organic carbon, providing critical feedstocks for heterotrophic organisms and supporting the larger oceanic ecosystem (5).

The core metabolic systems in *P. marinus* have diverged significantly from those of other cyanobacteria, due in part to genomic streamlining (6–10). Additionally, *P. marinus* lacks phycobilisomes, which are widely used by other cyanobacteria for light harvesting, and instead uses a divinyl chlorophyll a_2/b_2 complex (11). Furthermore, this cyanobacterium contains only one set of core photosystem components, while other cyanobacteria maintain several homologs (8, 12). Nitrogen assimilation pathways have been pruned, with species often lacking the ability to reduce either nitrate or nitrite (13, 14). Various ecotypes are incapable of heterotrophic growth, lacking several tricarboxylic acid cycle genes (8).

The life cycle of *P. marinus* is influenced by viruses. Cyanophages that infect *P. marinus* have evolved genomes with as many as 327 open reading frames (ORFs) (15). Viruses from three clades infect *P. marinus*, including T4-like myoviruses, T7-like podoviruses, and, less commonly, members of *Siphoviridae* (16). In some ecosystems, as many as 50% of cyanobacteria may be infected at any point in time (17). Some cyanophages exhibit infection cycles that are closely tied to day/night rhythms of cyanobacteria, although individual viruses vary in their responses (18). Once infection begins, many host genes are repressed in favor of phage homologs (19), which can decrease cyanobacterial carbon fixation, potentially keeping ~5 gigatons of carbon in the atmosphere (20). While recent estimates suggest that cyanophages are limited by energy rather than nutrients (21), our understanding of their controls over host electron transfer (ET) remains limited.

Following infection, cyanophages express metabolic genes to modulate host photosynthesis (22). Phage can express their own photosystem II (PSII) reaction core (D1 protein) during infection (17, 23, 24), with viral transcripts equaling or even exceeding host transcripts in some settings. Certain cyanophages encode an entire photosystem I (PSI) complex that is thought to be a more promiscuous oxidizer of electron carriers than host PSI, which may push host cells toward cyclic photosynthesis (25). Viral plastocyanin homologs, which possess altered charged surfaces, compared with host plastocyanin, can

This article contains supporting information.

* For correspondence: Jonathan J. Silberg, joff@rice.edu.

also be expressed and are thought to transfer electrons directly to cytochrome aa_3 oxidase rather than PSI as a mechanism for managing redox balance (26). Other phage genes implicated in oxygenic photosynthesis include *hli* (high-light-inducible protein), *pebA* (15,16-dihydrobiliverdin:Fd reductase), *psbD* (PSII D2 protein), *pcyA* (phycocyanobilin:Fd reductase), and *petF* (Fd) (15). Although the sequence similarities of these genes to their cyanobacterial homologs give clues to their cellular roles, we do not know how these proteins interact with host proteins to tune the host electron fluxome.

The *Prochlorococcus* P-SSM2 phage Fd (pssm2-Fd) supports the reduction of phage phycoerythrobilin synthase (PebS), which catalyzes the reduction of biliverdin IX_α to (*3E/3Z*)-phycoerythrobilin (27, 28). While prior studies showed that some Fds support ET to diverse partner oxidoreductases (29–32), it remains unclear how the partner specificity of this and other phage Fds compares with that of host Fds, which can function as ET hubs that couple light harvesting to a range of reductive metabolic reactions (31–33). In addition, it is not known how the primary structure and biophysical properties of phage Fds compare with those of host Fds.

In this study, we used a sequence similarity network (SSN) analysis to examine how cyanophage and cyanobacterial Fds relate to one another. We also determined the first structure of a cyanophage Fd, which has high structural similarity to cyanobacterial Fds. We show that this Fd has a low midpoint potential characteristic of photosynthetic Fds, we establish that this protein has a low thermostability (T_m = 28 °C), and we show that it supports ET to a host oxidoreductase involved in sulfur assimilation. These results suggest that viral Fds support ET to cyanobacterially encoded oxidoreductases, and they extend our understanding about the ways in which viruses interact with cyanobacterial hosts.

Results

Cyanophage and host Fd bioinformatics

To better understand the prevalence of cyanophage Fds, we searched all 8392 viral genomes available in the Integrated Microbial Genomes and Microbiomes database for ORFs matching the InterPro signature for [2Fe-2S] Fds (34). This genome mining yielded 26 Fds from phages that have been shown to infect *Prochlorococcus* and *Synechococcus* (including pssm2-Fd), a Fd from an uncultured marine virus, and a Fd from the giant *Pseudomonas* phage OBP (35). All viral ORFs encoded Fds with 95–97 residues, with the exception of the *Pseudomonas* phage OBP, which encoded 83 residues.

SSNs represent a simple way to visualize how protein paralogs relate to one another in their primary structure, and they provide a frame of reference for establishing how phage-encoded proteins might have evolved from host proteins. Additionally, the individual clusters in these networks often include protein homologs with similar functional properties (36), so they can provide hints about the possible functions of phage-encoded proteins. To understand which cyanobacterial Fds are most closely related to phage Fds, we used an SSN to compare viral Fds with 807 cyanobacterial Fds obtained from a recent genome-mining effort (37). *Zea mays* Fd1 (zm-Fd1) was included for a frame of reference, because this protein has been intensively studied (38, 39). When the Fds were compiled into a SSN (40), the cyanobacterial Fds presented over a dozen distinct clusters, which arose because of variation in Fd length (Fig. 1*A*). Across the 12 largest clusters, the average Fd length varied by ~100 amino acids. These clusters also vary in the number of cyanobacterial species represented and the average Fd size, with the top five most species-diverse clusters being VI (100 ± 8 residues), IX (115 ± 9 residues), VII (106 ± 13 residues), I (79 ± 2 residues), and XI (163 ± 8 residues) (Dataset S1).

The phage Fds all localize to Cluster VI, in close association with cyanobacterial Fds (Fig. 1*B*), with the exception of *Pseudomonas* phage OBP Fd, which does not cluster with any Fds. Cluster VI includes numerous structurally characterized Fds, including Fds from *Synechocystis* sp. PCC 6803 (s6803-Fd1), *Nostoc* sp. PCC 7119 (nsp-Fd1), *Thermosynechococcus elongatus* (te-Fd1), and *Mastigocladus laminosus* (ml-Fd1). Additionally, this cluster contains zm-Fd1, the Fd included for a frame of reference.

Among the Fds in Cluster VI, interactions with a range of oxidoreductases have been documented. s6803-Fd1 binds PSI, glutamate synthase, and Fd-NADP reductase (FNR) (41–43). nsp-Fd1 interacts with FNR (44). te-Fd1 interacts with FNR, PSI, heme oxygenase, PcyA, nitrite reductase (NIR), and 4-hydroxy-3-methylbut-2-enyl diphosphate synthase (45–48). The latter oxidoreductase is in the nonmevalonate pathway for isoprenoid biosynthesis (47). The tight association of cyanophage and cyanobacterial Fds having a wide range of protein-protein interactions suggested that cyanophage Fds might be able to support ET to host oxidoreductases. Given that sulfite reductase (SIR) and NIR have similar sequences, possess related folds, and utilize the same cofactors, we reasoned that cyanophage Fds could interact with SIR (38, 49, 50). pssm2-Fd is encoded by a myophage that infects *P. marinus*. By analogy to characterized host Fds, it has the potential to interact with a total of eight host oxidoreductases (Fig. 1*C*), in addition to the virally encoded PebS (15, 27, 51).

pssm2-Fd contains sequence features of host Fds

To better understand how the pssm2-Fd structure relates to cyanobacterial Fds, we analyzed the pairwise sequence identity of pssm2-Fd and cyanobacterial Fds in *P. marinus* hosts infected by cyanophage P-SSM2 (51). Fds from three host strains were collected by protein BLAST and designated pmN1-Fd1 (ecotype NATL1A), pmN2-Fd1 (NATL2A), and pm9211-Fd1 (MIT9211) (52). Like pssm2-Fd, these Fds reside within Cluster VI. We also evaluated the pairwise identity of pssm2-Fd with structurally characterized Fds, including cyanobacterial (s6803-Fd1, nsp-Fd1, te-Fd1, and ml-Fd1) and plant (zm-Fd1) Fds. This analysis revealed that most (5 of 7) cyanobacterial Fds exhibited ≥70% identity with each other (Fig. 2*A*), while pssm2-Fd exhibited a range of sequence identities with these Fds (40–60%). Interestingly, pssm2-Fd presented slightly higher sequence identities with Fds from nonhost cyanobacteria than from host cyanobacteria. The Fds from *P. marinus* ecotypes NATL1A and NATL2A (pmN1-Fd1 and pmN2-Fd1)

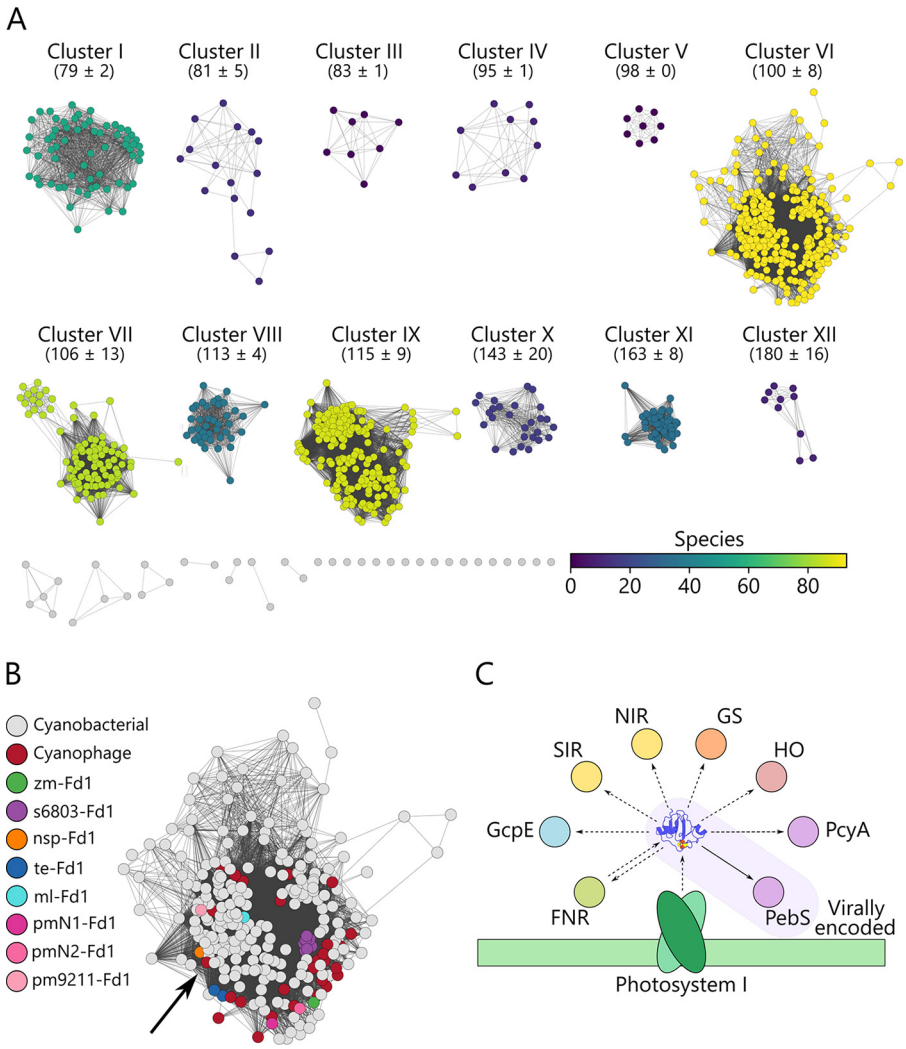

Figure 1. Network analysis of cyanophage and cyanobacterial Fds. *A*, a network illustrates the relationships of 807 cyanobacterial and 28 cyanophage Fds. Edges were drawn between Fd pairs that exhibited a sequence alignment score of ≥30. For the largest clusters (Clusters I–XII), the average protein lengths encoded by the ORFs in the cluster are provided ±1σ. Clusters are colored using a viridis gradient, according to the number of species represented in each cluster. *B*, cyanophage and cyanobacterial Fds are highlighted within Cluster VI, with zm-Fd1 for a frame of reference. The *arrow* indicates pssm2-Fd. Fds from multiple species and strains share the same sequence as s6803-Fd1 and te-Fd1, so they are all colored identically. *C*, *P. marinus* partner oxidoreductases that have the potential to interact with pssm2-Fd during an infection. *GcpE*, 4-hydroxy-3-methylbut-2-enyl diphosphate synthase; *GS*, glutamate synthase; *HO*, heme oxygenase.

exhibited the lowest identity with pssm2-Fd (43%) and appeared to be the two most divergent Fds in the set. pm9211-Fd1 exhibited higher sequence identity with pssm2-Fd (52%) and appeared more closely related to other cyanobacterial Fds (s6803-Fd1, te-Fd1, nspFd1, and ml-Fd1) than the other *P. marinus* ecotypes.

Fd binding specificities are influenced by charged surface residues and residues that make direct contacts with partner proteins (38, 39). To establish whether the pssm2-Fd sequence is conserved at positions implicated in forming residue-residue contacts with partner proteins, a multiple sequence alignment was generated (Fig. 2*B*). Residues implicated in contacting Fd partners from crystal structures of Fd-partner complexes are highlighted (38, 39, 45). In the case of the Fd-FNR complex (PDB code 1GAQ), all of the Fd residues that make contacts with FNR are completely conserved (39), suggesting a ubiquitous strategy for binding to FNR across cyanobacteria. For the Fd-PSI complex (PDB code 5ZF0) and Fd-SIR (PDB code 5H92), greater variability is observed in the Fd residues that mediate partner contacts (38, 45). Only 8 of the 11 Fd residues that contact PSI are either absolutely conserved or have residues with similar physicochemical properties. Similarly, 4 of the 6 Fd residues that contact SIR are either absolutely conserved or similar.

pssm2-Fd is marginally stable

The tight association of pssm2-Fd with cyanobacterial Fds in Cluster VI suggested that these proteins may exhibit similar biophysical properties. To obtain recombinant pssm2-Fd for *in vitro* characterization, the gene encoding pssm2-Fd was overexpressed in *Escherichia coli* at 37 °C and purified using a combination of anion exchange and size exclusion chromatography. This protocol yielded 0.6 mg/liter phage Fd, which was estimated to be >95% homogeneous by SDS-PAGE analysis. This

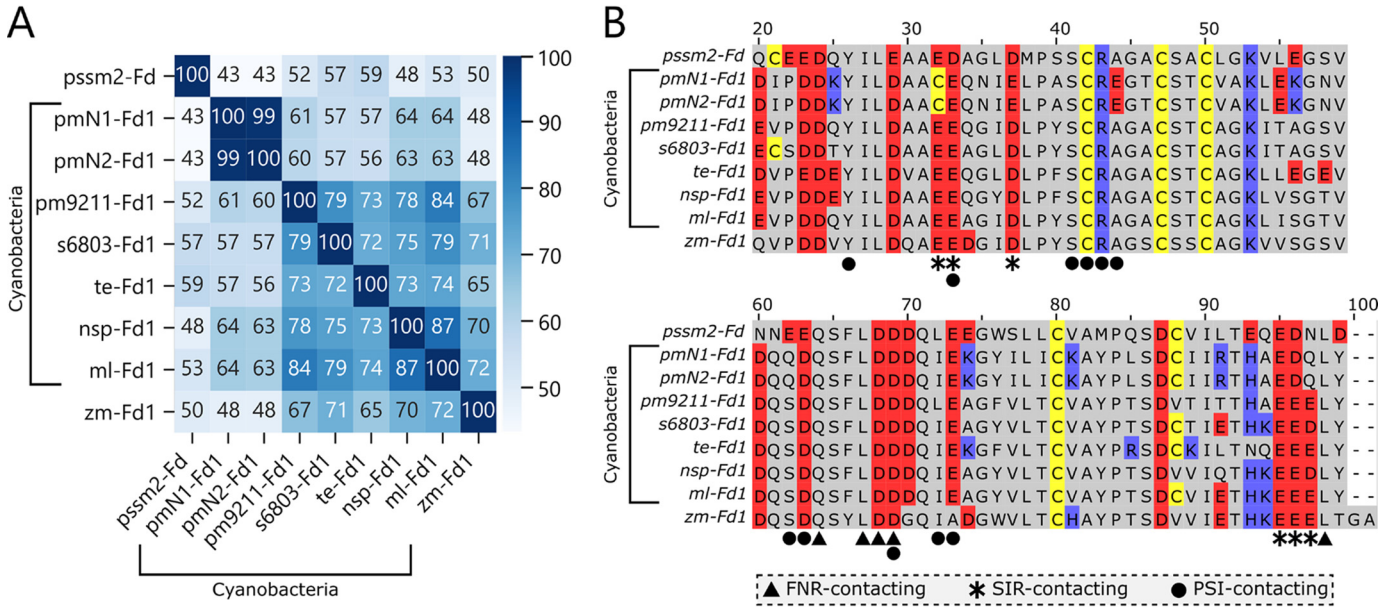

Figure 2. Cyanophage and host cyanobacterial Fd sequence comparisons. *A*, a matrix shows the pairwise sequence identity of pssm2-Fd and Fds from host cyanobacteria, cyanobacteria with known structures, and one plant family member (zm-Fd1). The *blue shading* indicates the percent sequence identity. *B*, a multiple sequence alignment illustrates the conservation of cysteines (*yellow*), positively charged residues (*blue*), negatively charged residues (*red*), and residues implicated in binding to FNR, SIR, and PSI (38, 39, 45). Residues are indexed with respect to ml-Fd1.

yield is ~25-fold lower than that obtained with a thermophilic cyanobacterial Fd using an identical expression protocol (53).

To determine whether pssm2-Fd contains a [2Fe-2S] cluster, we acquired pssm2-Fd absorbance and circular dichroism (CD) spectra (Fig. 3, *A* and *B*). The absorption spectrum contains peaks (465, 420, and 330 nm) that are characteristic of holo-Fds (54, 55). Additionally, the CD spectrum presented ellipticity maxima (427 and 360 nm) and minima (550 and 505 nm) that are observed with holo-Fds (54, 55). The ratio of the ellipticity at 427 nm to the pssm2-Fd concentration was comparable to that of a previously purified *Azotobacter vinelandii* Fd that had nearly stoichiometric cluster occupancy (56). This finding suggests that a significant fraction of pssm2-Fd contains a [2Fe-2S] cluster.

Because the yield of pssm2-Fd was lower than that of a thermophilic Fd that we recently purified (53), we postulated that pssm2-Fd might have a lower T_m. Iron-sulfur clusters often stabilize Fd structures, and in some cases they degrade only after some secondary structure is lost (57, 58). Because a [2Fe-2S] moiety is required for Fd ET and cluster loss often leads to irreversible folding, we evaluated the effect of temperature on pssm2-Fd by measuring the ellipticity (at 427 nm) that arises from iron-sulfur cluster binding (Fig. 3*C*) (59, 60). Assuming two-state unfolding (61), the fraction of folded pssm2-Fd at each temperature was analyzed in a Van't Hoff plot. A linear fit of this plot yielded $\Delta H_{unfolding}$ and $\Delta S_{unfolding}$ (Fig. S1), which were used to calculate a T_m of 28 °C.

To determine how the midpoint potential of pssm2-Fd relates to photosynthetic Fds, we characterized the electrochemical properties of this Fd using thin-film, square wave voltammetry (62). With this analysis, pssm2-Fd presented a low midpoint potential (E_m = −336 mV), relative to a standard hydrogen electrode (Fig. 3*D*), a value that is similar to the values observed in photosynthetic Fds.

Cyanophage Fd structural characterization

We determined the pssm2-Fd crystal structure at 1.6-Å resolution. The resulting model (R_{cryst} = 0.180; R_{free} = 0.213) contains all 96 residues for each of the two monomers in the asymmetric unit, excluding the initiator methionines. The two subunits in the asymmetric unit superposition well, with a low root mean square deviation (RMSD) of all atomic coordinates (0.17 Å). The main source of variation between the chains arises from subtle differences within the β-sheets. While Chain A in the asymmetric unit is well ordered, Chain B has weaker density for residues around the iron-sulfur cluster, with a poor fit to the electron density, resulting in a large real-space *R* value in this region. Therefore, noncrystallographic symmetry restraint refinements were carried out using Chain A as a reference for Chain B. Additionally, Chain A has density that is consistent with a [2Fe-2S] cluster, while the same region of Chain B has density that reflects a mixture of zinc and a [2Fe-2S] cluster. This observation is likely due to the zinc present under crystallization conditions. Evidence in the literature indicates that zinc can interfere with and disrupt iron-sulfur clusters (63–66). To account for the poor density and the anomalous data, Chain B was modeled with grouped occupancies, in which the model is a mixture of an intact cysteine-coordinated iron-sulfur cluster and a zinc ion with a hydration shell. An interpretation of these data is that, as the cluster is disrupted, the surrounding residues become disordered. The crystallographic data collection and refinement statistics are provided in Table S1.

The structure of the pssm2-Fd is shown in Fig. 4*A*, With five β-sheet strands and three α-helices, pssm2-Fd possesses a canonical β-grasp topology, which consists of a β-sheet that is 4–5 strands long with α-helices interspersed and packed against the sheet (67). This topology is observed in other Fds, such as

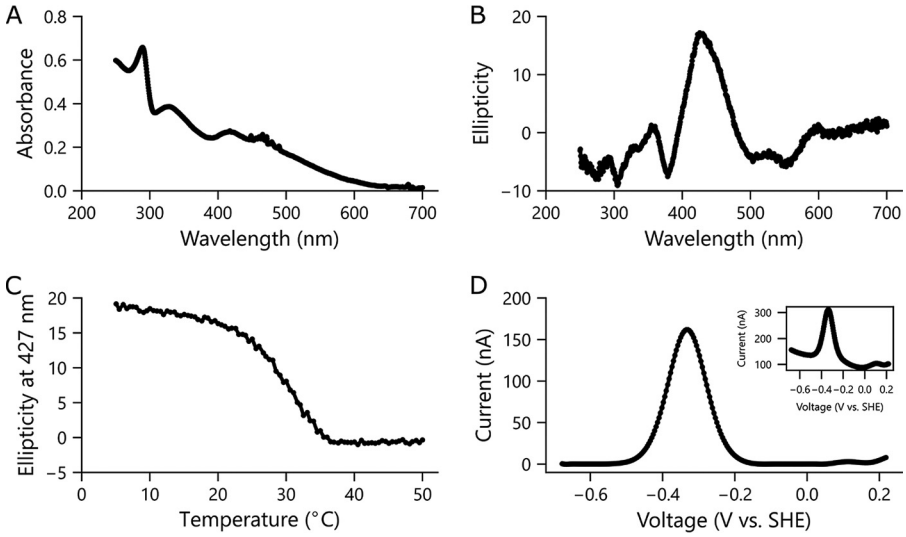

Figure 3. Biophysical properties of purified pssm2-Fd. *A* and *B*, absorbance and CD spectra of purified pssm2-Fd (50 μM) dissolved in TED buffer (25 mM Tris pH 8, 1 mM EDTA, and 1 mM DTT), revealing features characteristic of [2Fe-2S] Fds. *C*, effect of temperature on the ellipticity of pssm2-Fd (50 μM) in TED buffer at 427 nm. The midpoint of the transition occurs at 28 °C. *D*, square wave voltammetry of pssm2-Fd (620 μM) in 5 mM acetate, 5 mM MES, 5 mM MOPS, 5 mM TAPS, 5 mM CHES, 5 mM CAPS, and 100 mM NaCl, pH 7, revealing a midpoint potential of −334 mV. *Inset*, voltammetry data prior to background subtraction.

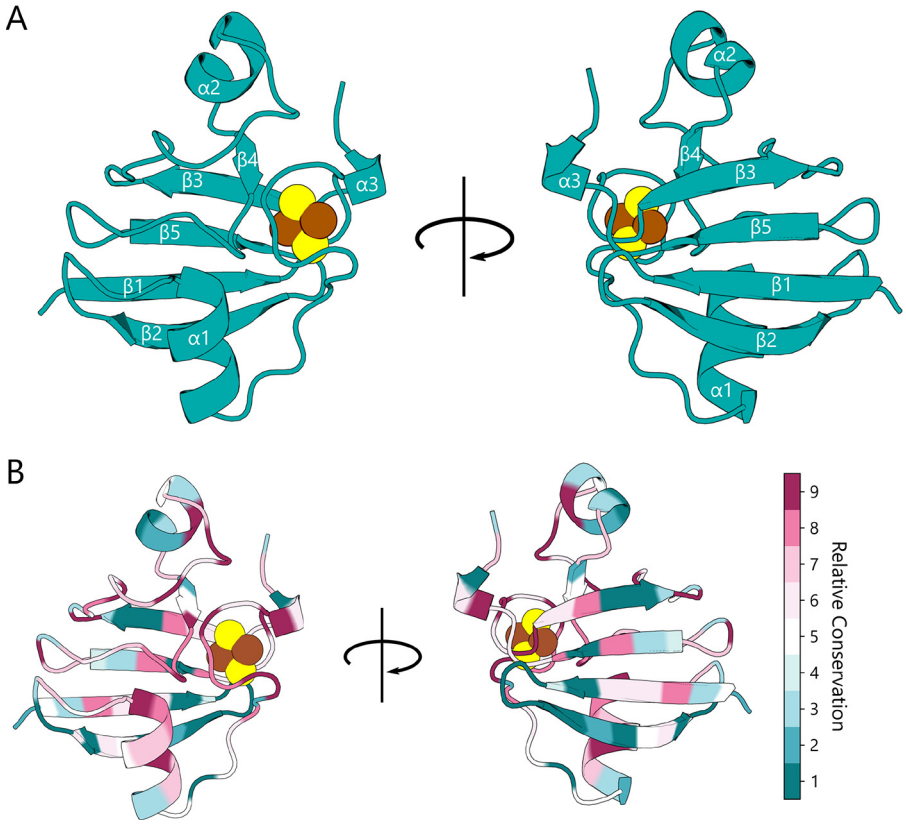

Figure 4. Phage Fd structure. *A*, front- and back-facing ribbon structures of the pssm2-Fd structure. Iron and sulfur atoms are shown as *brown spheres* and *yellow spheres*, respectively. The α-helices and β-sheet strands are labelled sequentially. *B*, ribbon structures of pssm2-Fd colored with ConSurf conservation scores generated using the Fds in Cluster VI. The most conserved residues are shown in *magenta*, while the least conserved residues are in *cyan*.

ml-Fd1 and s6803-Fd1 (41, 68). To quantify how similar the pssm2-Fd is to cyanobacterial Fds in Cluster VI (1OFF, 5AUI, 1CZP, 1RFK, and 3B2F), we calculated the pairwise RMSDs between these structures and Chain A of pssm2-Fd (41, 68–71). The pssm2-Fd structure presents low RMSDs ($\leq$0.5 Å) in all atom positions with the cyanobacterial Fds (Table S2), including two thermophilic Fds (45, 68) and a plant Fd (zm-Fd1). Given the high similarity of Chain A to other Fd

structures, we used this polypeptide for all subsequent structural analysis.

We next mapped the sequence variation of Fds within Cluster VI onto the pssm2-Fd structure (Fig. 4*B*). To quantify variation, we calculated the conservation scores at each pssm2-Fd residue using ConSurf (72). This analysis revealed that the greatest density of absolutely conserved residues occurs in the loop surrounding the [2Fe-2S] cluster, with the next most conserved regions being those adjacent to this loop. There are additional residues that are highly conserved across all of the Fds analyzed; however, these are dispersed across the structure and primarily localized to regions that are packed within the center of the pssm2-Fd structure or form salt bridges on the surface.

Analysis of the intramolecular interactions within pssm2-Fd and those observed within cyanobacterial Fds found in Cluster VI revealed additional differences (Table S2). Among the proteins analyzed, pssm2-Fd presents a lower number of salt bridges (n = 3), compared with all other Fds analyzed (n = 4–6). However, pssm2-Fd contains a similar number of total hydrogen bonds (n = 133), compared with the other Fds (n = 105–154). Only 1 salt bridge was conserved in all of the Fds, which arises from an interaction between an arginine at alignment position 43 and either a glutamate or an aspartate situated between position 29 and position 32. This interaction may be conserved because it helps shape the [2Fe-2S] cluster-binding loop, as the arginine is directly adjacent to a cluster-ligating cysteine (Fig. 2*B*).

pssm2-Fd supports ET to a host SIR

In a previous study, we examined whether pssm2-Fd could support ET between *Zea mays* FNR (zm-FNR) and SIR (zm-SIR) using a synthetic ET pathway in *E. coli* that is required for cellular growth (53). In this assay, Fd-mediated ET from FNR to SIR is required for sulfur assimilation and growth on medium containing sulfate as the only sulfur source (Fig. 5*A*) (73). The prior study found that pssm2-Fd could not support ET from zm-FNR to zm-SIR (53). However, those experiments were performed at 37 °C, at which only a small fraction of pssm2-Fd is folded.

To increase the fraction of holo-pssm2-Fd in the cellular assay, we built an anhydrotetracycline (aTc)-regulated expression vector that initiates translation of pssm2-Fd using a synthetic ribosome-binding site with strong translation initiation. When the assay was performed using this vector, aTc-dependent complementation was observed at 37 °C (Fig. 5*B*). This finding indicates that pssm2-Fd supports ET from zm-FNR to zm-SIR but requires high levels of protein expression to compensate for the low stability of pssm2-Fd.

To test whether pssm2-Fd can also support ET to host SIRs, we created vectors that constitutively express *P. marinus* NATL2A SIR (pmN2-SIR) and MIT9211 SIR (pm9211-SIR) in parallel with zm-FNR. SIR from the NATL1A host was omitted because it shares high sequence identity (98%) with pmN2-SIR (Fig. S2). Analysis of the zm-Fd1/zm-SIR complex structure revealed that these *P. marinus* SIRs are identical to zm-SIR at 5 of the 7 residues that bind zm-Fd1 (Fig. S3) (38). We also built aTc-inducible vectors to express host Fds (pmN1-Fd1, pmN2-Fd1, and pm9211-Fd1). Using these vectors, we tested the ability of cyanophage and host Fds to support ET from zm-FNR to zm-SIR and from zm-FNR to two host SIRs (pmN2-SIR and zm-9211-SIR). Because ml-Fd1 supports ET from zm-FNR to zm-SIR (53), it was included in the analysis as a positive control. Assays were performed at 23, 30, and 37 °C with and without aTc, which regulates Fd expression.

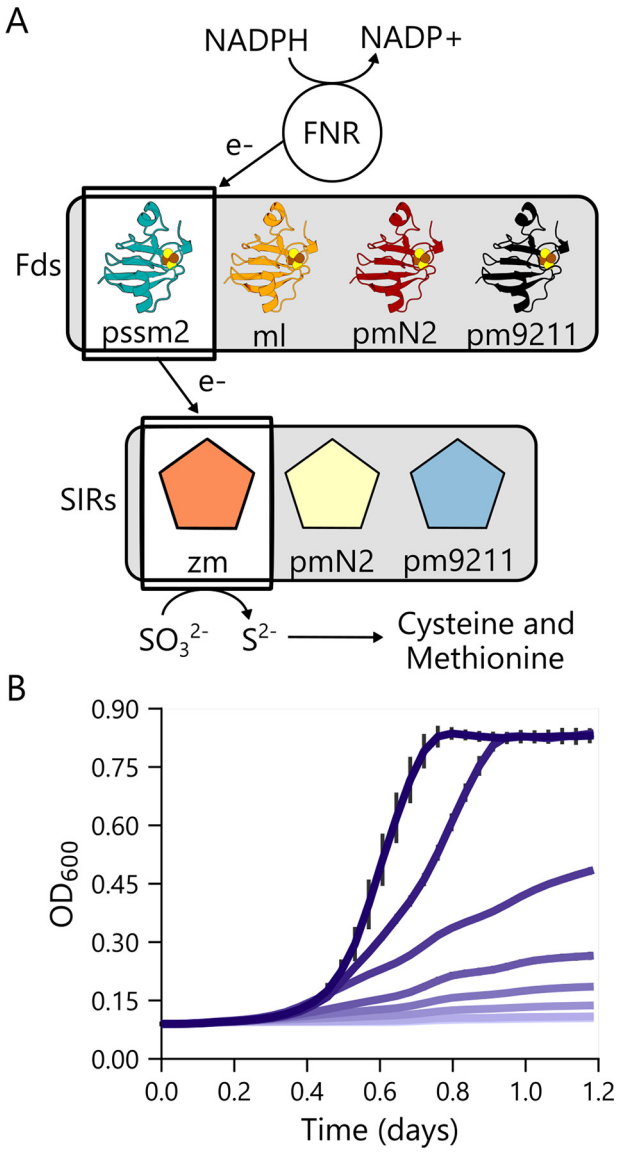

Figure 5. Monitoring of pssm2-Fd ET using a cellular assay. *A*, an *E. coli* auxotroph unable to produce sulfide can grow on sulfite as a sulfur source when cells express a three-component pathway consisting of FNR, Fd, and SIR. In this study, four different Fds and three different SIRs were examined. *B*, the effect of aTc concentration on the growth complementation of *E. coli* EW11 transformed with vectors that express pssm2-Fd using an aTc-inducible promoter and zm-FNR/zm-SIR using constitutive promoters. The aTc concentrations (0, 1.6, 3.1, 6.3, 12.5, 25, 50, and 100 ng/ml) are color coded as a gradient from *light purple* (no aTc) to *dark purple* (highest aTc). Average values from three biological replicates are shown, with *error bars* representing $\pm 1\sigma$.

At the highest temperature assayed (37 °C), only cells expressing zm-SIR complemented growth when coexpressed with a Fd and FNR (Fig. 6*A*). This growth was observed with ml-Fd1, pssm2-Fd, and pm9211-Fd1. Cells expressing pmN2-Fd did not support ET from zm-FNR to zm-SIR. At 30 °C, complementation was again observed with the same three-

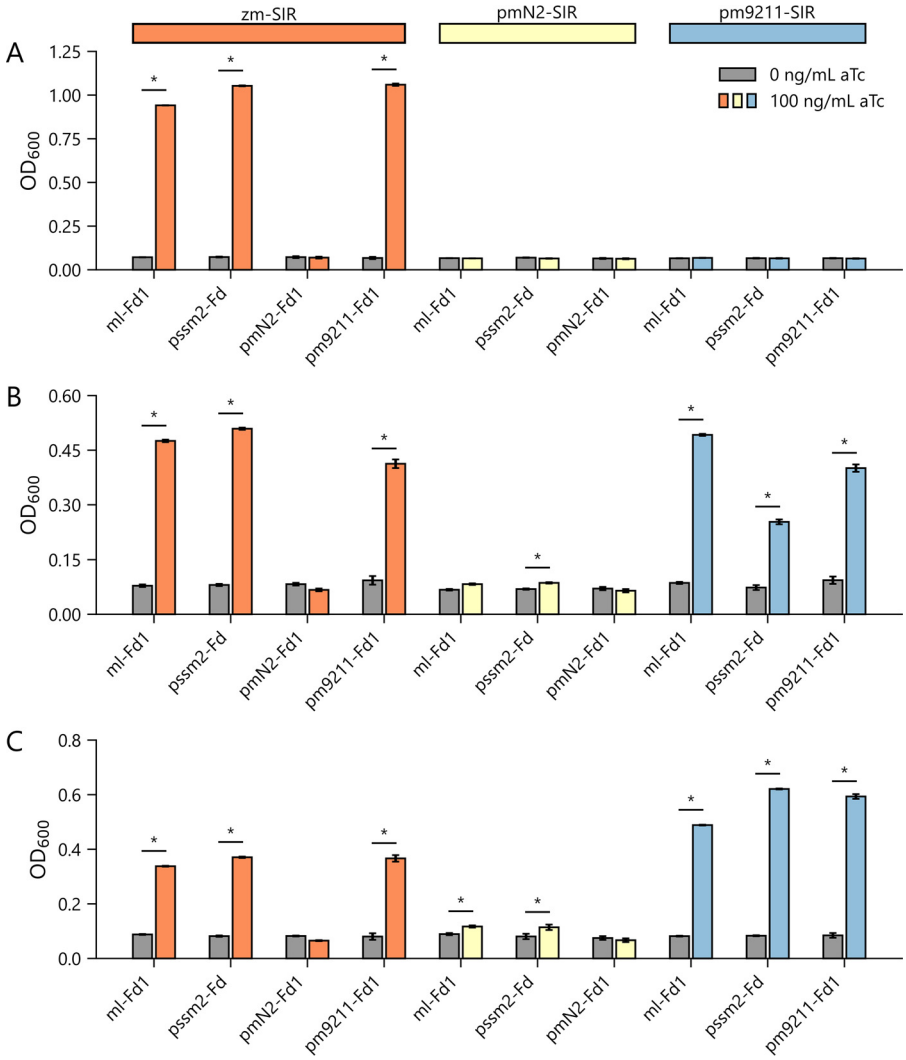

Figure 6. pssm2-Fd supports ET to host SIRs. Growth complementation observed at 37 °C (*A*), 30 °C (*B*), and 23 °C (*C*) with *E. coli* EW11 cells transformed with vectors that constitutively express zm-FNR with three different SIRs (zm-SIR, pmN2-SIR, and pm9211-SIR) and a vector that uses an aTc-inducible promoter to express different Fds (ml-Fd1, pssm2-Fd, pmN2-Fd1, and pm9211-Fd1). Experiments were performed in the absence (*gray bars*) and presence (*colored bars*) of 100 ng/ml aTc to evaluate the dependence of growth on Fd expression. *Error bars* represent $\pm 1\sigma$ from three biological replicates. For each strain, an independent two-tailed *t* test was used to compare the OD_{600} in the absence and presence of aTc ($\alpha = 0.05$). Significant differences are noted with *asterisks*.

component ET pathways (Fig. 6*B*). Additionally, cells expressing pm9211-SIR complemented growth when coexpressing zm-FNR and either the cognate host Fd, pssm2-Fd, or ml-Fd1. At 23 °C, trends similar to those at 30 °C were observed with zm-SIR and pm9211-SIR (Fig. 6*C*). Additionally, significant complementation, albeit small, was observed when pmN2-SIR was coexpressed with pssm2-Fd and ml-Fd1.

To investigate whether differences in Fd-dependent growth arise because the Fds are expressed at different levels, we created expression vectors that produce these proteins as fusions with red fluorescent protein (RFP). We performed whole-cell fluorescence measurements using cells transformed with these vectors and compared the signals with those for cells expressing ml-Fd1 alone (Fig. 7). This analysis revealed that pmN2-Fd is expressed at higher levels than the other three Fds under the expression conditions used for the cellular assay. This finding suggests that the weaker complementation observed with pmN2-Fd does not arise because it is expressed at lower levels than the Fds that complement growth.

To evaluate whether variability in structural properties correlates with cellular complementation, we evaluated the surface charge distribution of Fd and SIR structures (zm-Fd1, PDB code 3B2F; pssm2-Fd, PDB code 6VJV; zm-SIR, PDB code 5H8V), as well as structural models for Fds and SIRs lacking structures (pmN2-Fd1, pm9211-Fd1, pmN2-SIR, and pm9211-SIR) (38, 71). With the Fds that complement corn SIR, we observed similar charge distribution proximal to the iron-sulfur cluster (Fig. 8*A*). Notably, the host Fd that did not support cellular ET to corn SIR (pmN2-Fd1) is the least electronegative Fd. When we analyzed the charge distribution of the SIRs, we observed similar surface charges, with slightly more electronegative character in cyanobacterial SIRs, compared with zm-SIR (Fig. 8*B*).

Discussion

Our bioinformatic analysis reveals how phage Fd relates to the different Fd paralogs in cyanobacteria. Twelve major clusters of cyanobacterial Fds were observed, with some clusters

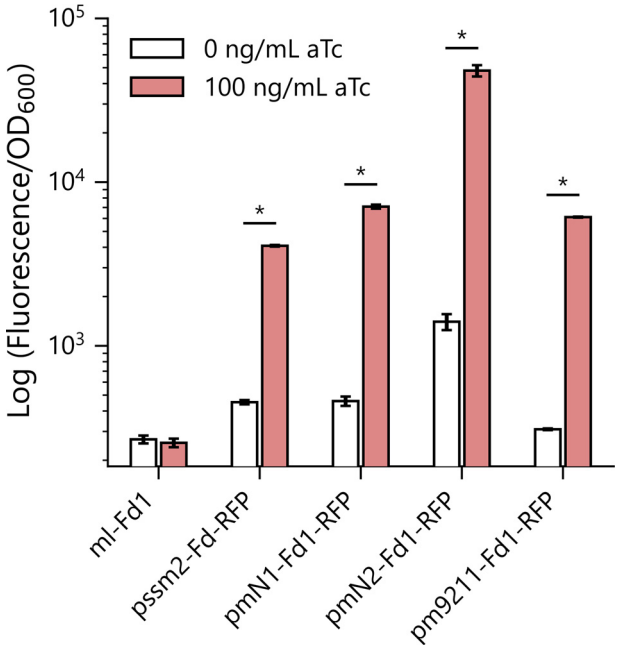

Figure 7. Expression of Fd-RFP fusion proteins. Fluorescence was measured in *E. coli* EW11 cells transformed with vectors that express Fds using an aTc-inducible promoter. Cells were grown under nonselective conditions. For each strain, an independent two-tailed *t* test was used to compare fluorescence normalized to the OD_{600}, with or without aTc ($\alpha = 0.05$). *Error bars* represent $\pm 1\sigma$ from three biological replicates. Significant differences are noted with *asterisks*.

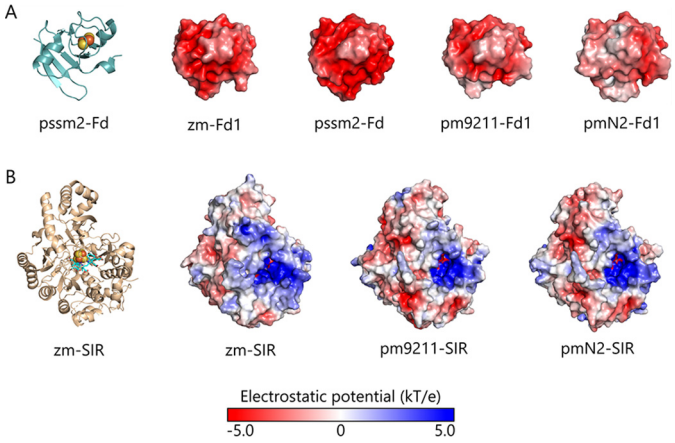

Figure 8. Comparison of the electrostatic potential surfaces of Fds and SIRs. The surfaces of Fd (*A*) and SIR (*B*) homologs are colored according to electrostatic potential, ranging from *blue* to *red* (*kT*/*e*), where *kT* is thermal energy and *e* is the elementary charge. zm-Fd1, pssm2-Fd, and zm-SIR were generated using crystal structure data, while all other structures represent homology models (38, 71). The front faces of the Fds are negatively charged to various degrees, while the SIRs display positive binding surfaces with small variations. These oppositely charged patches interact during binding, bringing the metallocofactors from each protein into close proximity to facilitate ET (38). Iron-sulfur clusters are displayed as *spheres* and sirohemes as *sticks*.

representing Fds that are widespread across cyanobacteria and others containing Fds from a small number of organisms. Only a small subset of the Fds in the network have been characterized. In the case of the cyanobacterial Fds in Cluster VI, which includes all of the cyanophage Fds, several of these proteins represent Fds expressed under phototrophic conditions (31, 74, 75). In some cases, this expression is likely due to their critical role as the electron acceptor for PSI (42, 45). Since Cluster VI contains cyanobacterial Fds that have evolved to support ET to a wide range of oxidoreductases, it seems likely that cyanophage Fds arose from the duplication of a cyanobacterial Fd that mediates ET to one or more of these partner oxidoreductases.

A comparison of biochemical studies in *Synechocystis* sp. PCC6803 with our bioinformatics suggests that the clusters represent Fd paralogs with distinct cellular roles. This organism has Fd paralogs that map to Clusters V, VI, IX, and X (31). The variable regulation of these Fds supports the idea that these proteins have distinct cellular roles (31, 74, 76). Transcripts encoding many of these Fd paralogs are regulated by environmental conditions, with changes in gene expression being observed in response to salt stress, high metal concentrations, low light, and blue light. Despite this knowledge, we know little about the partner specificity profiles of Fds outside Cluster VI.

Our bioinformatics revealed some additional trends across the clusters. Clusters I and II consist of mini-Fds with tight size distributions ($\mu = 79 \pm 2$ and $\mu = 81 \pm 5$ amino acids, respectively) and a tryptophan at the C terminus. This is an unusual feature, compared with canonical Fds in Cluster VI, which generally end with a tyrosine. The tryptophan-terminating Fds are found in >40 cyanobacteria, although Cluster II consists wholly of *Prochlorococcus* and *Synechococcus* Fds. Structures of these Fds have not yet been reported. The only structurally characterized [2Fe-2S] Fd with a terminal tryptophan is a cytochrome P450-reducing homolog from *Pseudomonas putida* (1PDX), but it is 106 amino acids long and much larger than the Fds within Clusters I and II (77).

Some of the clusters in our network represent Fds that are unique to specific cyanobacterial species. Cluster III is solely populated by Fds from *P. marinus* ecotypes, which are not known to be infected by P-SSM2 cyanophage. Cluster V contains only Fds from *Synechocystis* strains. Finally, Cluster X is populated primarily by Fds from *P. marinus* and *Synechococcus* sp. strains, although it also contains two species of *Cyanobium*. Future studies will be required to better understand how sequence variation within and across clusters relates to the evolution of partner specificity profiles across different cyanobacteria.

Our biophysical analysis revealed that phage Fd exhibits a similar overall structure compared with nonhost cyanobacterial Fds found in Cluster VI (41, 68–70), presenting RMSDs of ≤0.5 Å with respect to mesophilic (nsp-Fd1 and s6803-Fd1) and thermophilic (te-Fd1 and ml-Fd1) Fds. Our electrochemical measurements showed that the pssm2-Fd has a potential on the high range of those observed in Cluster VI, which have midpoint potentials that range from −412 to −336 mV (53, 78, 79). How the structures and electrochemical properties of *P. marinus* Fds relate to pssm2-Fd is not known. However, given the similarity of the phage Fd structure to those of more distantly related Fds, it seems likely that they will be similar to those of characterized orthologs in other cyanobacteria that serve as PSI electron acceptors.

Our biochemical studies showed that pssm2-Fd has a low melting temperature ($T_m = 28$ °C) compared with the other Fds in Cluster VI, including the thermophilic ml-Fd1 (80). This

melting temperature is greater than the range (15–25 °C) at which the *P. marinus* hosts grow (4). This low T_m might have been selected to support more rapid turnover of cyanophage Fds or to regulate protein turnover in response to temperature changes. Currently, it is not known how Fds tune their stability without altering their midpoint potential. The native residues that control Fd stabilities (T_m = 28–76 °C) could be established in future studies by creating chimeras between pssm2-Fd and more thermostable Fds with similar midpoint potentials and then evaluating how inheritance of different native residues relates to the thermostability of the resulting chimeras (81, 82).

Our cellular measurements suggest that cyanophages may need to support host sulfur metabolism to maximize their fitness. The underlying need for this ET is not known, but it might have arisen because sulfur-containing amino acids are required for translation of phage proteins under conditions in which reduced sulfur is scarce. In *P. marinus* ecosystems, daytime dissolved dimethylsulfoniopropionate and methionine levels reach only 0.5–10 nM and 10–40 pM, respectively (83–85). In addition, methionine levels peak during the day and drop below detection limits after sunset, suggesting that the diurnal cycle of cyanobacteria contributes to sulfur cycling in surface communities (84). In contrast, oxidized sulfur like sulfate is abundant, at 28 mM (83), and can be readily assimilated through a SIR-dependent pathway. Thus, cyanophages may use their Fd to support ET through this pathway under conditions in which reduced sulfur becomes limiting to the production of phage proteins or other sulfur-containing metabolites critical for phage fitness.

The relative preference of phage Fd for host- *versus* phage-encoded oxidoreductases will be interesting to explore in future studies. One way to address this competition would be to examine how coexpression of the phage Fd-partner PebS and host SIR affects growth complementation in our cellular assay. The advantage of this synthetic biology approach over more traditional *in vitro* methods is that it would allow higher-throughput analysis of protein-protein interactions in the crowded environment of a cell. Additionally, this approach could be applied to other natural and engineered Fds that support cellular ET from FNR to SIR (53, 86, 87).

Experimental Procedures

Materials

Tris was from Fisher Scientific, CAPS was from Acros Organics, MES and TAPS were from Fluka Biochemika, and IPTG, DTT, kanamycin, chloramphenicol, and streptomycin were from Research Products International. MOPS, CHES, and all other chemicals were purchased from Sigma-Aldrich. *E. coli* EW11 was a gift from Pam Silver (Harvard University) (73), *E. coli* XL1-Blue was from Agilent, and Rosetta(DE3) was from Novagen.

Vector design

All plasmids are listed in Table S3. Genes were synthesized by Integrated DNA Technologies or Twist Bioscience as gBlocks or gene fragments, respectively. Plasmids were constructed by ligating PCR products amplified with Q5 polymerase (New England Biolabs) using Golden Gate assembly (88). Translation initiation sites were designed using the ribosome-binding site calculator (89). All plasmids were sequence verified.

Bioinformatics

To harvest viral Fd ORFs, all available viral genomes from Integrated Microbial Genomes and Microbiomes (n = 8392) were scanned for genes encoding Fds with the InterPro signature IPR001041 (34). Viral genes with this signature were compiled with the 807 cyanobacterial [2Fe-2S] Fds listed in Dataset S1. To obtain pairwise sequence similarity scoring and to generate a SSN, these Fds were analyzed using the Enzyme Function Initiative-Enzyme Similarity Tool (36). The resulting networks were analyzed and images were generated using Cytoscape with the prefuse force-directed layout, based on an alignment score cutoff of 30 (90). Protein sequence alignments were generated using MUSCLE (91).

Protein purification

E. coli Rosetta cells transformed with pJTA022 were grown to exponential phase at 37 °C in lysogeny broth containing 50 μg/ml kanamycin, induced with 50 μM IPTG, and grown overnight at 37 °C with shaking at 250 rpm. Cells harvested by centrifugation (4000 × *g*) were resuspended in 25 ml of lysis buffer/liter of culture, which contained 10 mM Tris, pH 8, 5 mM DTT, 10 mg/liter DNase I, and 0.5 mg/ml lysozyme. After freezing at −80 °C, cells were thawed and mixed with a cOmplete Mini, EDTA-free, protease inhibitor tablet (Sigma-Aldrich) at a ratio of 1 tablet/100 ml of lysate. Samples were kept on ice or at 4 °C for all subsequent purification steps. Clarified lysate generated by centrifugation (47,000 × *g*) was diluted 3-fold with TED buffer (25 mM Tris, pH 8, 1 mM EDTA, and 1 mM DTT) to lower the salt concentration. This mixture was loaded onto a DE52 column (Whatman), the column was washed with TED buffer containing 200 mM NaCl, and the Fd was eluted using sequential isocratic washes with TED buffer containing 250 and 300 mM NaCl. Fractions appearing brown were mixed and diluted with TED buffer to bring NaCl below 100 mM. These pooled fractions were loaded onto a HiTrap Q XL column (GE Healthcare) using an AKTA Start FPLC system (GE Healthcare). The column was washed using 100 ml of TED buffer. Protein was eluted using a linear gradient (0–375 mM NaCl in TED buffer), followed by an isocratic wash (500 mM NaCl in TED buffer). Brown fractions were pooled and then further purified using a HiLoad 16/600 Superdex 75 column containing TED buffer. SDS-PAGE was performed to analyze the purity at each step, using NuPAGE 12% bis-Tris gels (Invitrogen) and the PageRuler unstained broad-range protein ladder (Thermo Fisher Scientific). Samples appearing homogeneous were pooled, concentrated using an Amicon Ultra 10-kDa-cutoff spin column, and then flash frozen with liquid nitrogen. Following stability measurements, protein expression was evaluated at 25 °C in terrific broth. When protein was purified following low-temperature expression, the final yield increased by 11.5-fold.

Spectroscopy

Prior to all measurements, pssm2-Fd was dialyzed into TED buffer. Absorbance spectra and ellipticity were acquired with a J-815 spectropolarimeter (Jasco, Inc.), using quartz cuvettes with a 1-cm path length. Scans used a bandwidth of 1 nm, a data pitch of 0.5 nm, and a scan rate of 200 nm/min, at 20 °C. To assess stability, a cuvette with 50 μM pssm2-Fd was heated from 5 °C to 50 °C at a rate of 1 °C/min while ellipticity was monitored at 427 nm.

Electrochemistry

Electrochemical measurements were performed anaerobically using a three-electrode system. An Ag/AgCl/1 M KCl electrode (CH Instruments) was used as the reference electrode, and a platinum wire was used as the counter-electrode. An edge-plane pyrolytic graphite electrode was used as the working electrode to perform protein film electrochemistry. Prior to the addition of Fd, this electrode was treated with 100 mM neomycin trisulfate (Sigma-Aldrich) to improve the electrochemical signal (92). A 3-μl aliquot of pssm2-Fd Fd (620 μM) was then applied to the electrode surface, and the protein was allowed to adhere for 1 min at 23 °C prior to placement in a glass vial containing a pH 7 buffer solution (5 mM acetate, MES, MOPS, TAPS, CHES, and CAPS) with 100 mM NaCl at 23.5 °C. Square wave voltammograms were collected at a frequency of 10 Hz, and electrochemical signals were analyzed using QSoas open software. Similar results were obtained when experiments were performed using pssm2-Fd from different purifications. A CH Instruments potentiostat and CHI660E electrochemical analyzer were used for all measurements. All data are reported relative to a standard hydrogen electrode, taking into account the potential difference between the standard hydrogen electrode and Ag/AgCl/1 M KCl, which is 0.222 V.

Crystallization

Purified pssm2-Fd (~20 mg/ml) was used for crystal screening with a mosquito LCP pipetting robot (SPT Labtech, Boston, MA) and commercially available screens including Wizard Classic 1 and 2 and Wizard Classic 3 and 4 (Rigaku Reagents, Inc., Bainbridge Island, WA), Morpheus and MIDAS (Molecular Dimensions, Holland, OH), and PEGRx and IndexHT (Hampton Research, Alisa Viejo, CA). Protein crystals were grown via the sitting drop method of vapor diffusion at a 1:1 (v:v) ratio of protein/precipitant (200 nl/200 nl), at 20 °C. Crystals for diffraction and data collection were optimized and grown with a precipitant solution containing 10% (w/v) PEG 3000, 200 mM zinc acetate, and 100 mM sodium acetate/acetic acid, pH 4.5. The crystals were cryoprotected with 10% glycerol, harvested using a MiTeGen micromesh loop (MiTeGen, Ithaca, NY), and flash-cooled in liquid nitrogen prior to data collection.

X-ray data collection, structure solution, and refinement

Data were collected at the Advanced Photon Source GM/CA beamline 23ID-B, using a 20-μm beam and 0.2° oscillations at a wavelength of 1.033 Å, with an Eiger X 16M detector (Dectris Ltd., Philadelphia, PA). The data were processed using the autoPROC toolbox (93), indexed and integrated using XDS (94), and scaled with AIMLESS (95). Initial phases were obtained by molecular replacement with Phaser-MR using the zm-Fd (PDB code 5H57) (96) as a search model. Model building and refinement were performed with Coot (97) and phenix.refine (98), respectively. A custom graphics system was used for collaborative visualization (99). Noncrystallographic symmetry restraints were used in initial refinements, with Chain A as a reference for Chain B, and were removed in the final rounds of refinement. For translation-tibration-screw refinement, groups were automatically determined for Chain A while Chain B was treated as one group. Anomalous difference maps were calculated using ANODE, and zinc from the precipitant solution was modeled in the structure (100). Data processing and refinement software were compiled and supported by the SBGrid Consortium (101). The structural model is available in the worldwide Protein Data Bank (PDB code 6VJV) (102). Data collection and refinement statistics are provided in Table S2.

Homology modeling

All-atom homology models were generated for pmN2-Fd1, pm9211-Fd1, pmN2-SIR, and pm9211-SIR using the fold and function assignment system (FFAS) server (103, 104). The Fe-S clusters for the Fd homology models were incorporated by aligning and copying them from our experimental model (PDB code 6VJV. The Fe-S clusters and sirohemes for the SIR homology models were incorporated by aligning the models to PDB code 5H8V and copying them.

Structural analysis

RMSDs were calculated, hydrogen bonds were detected (length cutoff, 3.5 Å), and structural images were generated using PyMOL (version 1.8; Schrödinger, LLC). The illustration of conserved Fd residues mapped onto the pssm2-Fd structure was generated using the ConSurf server with the WAG evolution model, seeded with all Fd sequences from Cluster VI (72). Electrostatic surface representations were calculated in PyMOL (version 2.3.2) using the APBS electrostatics plug-in with the prepwizard method default (Schrödinger). All solvent molecules, ions, and ligands were removed, while the Fe-S clusters and sirohemes were used in the map calculation.

Cellular assay

To assess Fd ET from FNR to SIR, *E. coli* EW11 was transformed with two plasmids using electroporation, as described (53, 73, 86, 87). One plasmid constitutively expresses FNR and SIR pairs, while the other expresses Fds under control of an aTc-inducible promoter. To maintain both plasmids, all growth steps included chloramphenicol (34 μg/ml) and streptomycin (100 μg/ml). Starter cultures inoculated using single colonies were grown in deep-well 96-well plates for 18 h at 37 °C, in 1 ml of a nonselective modified M9 medium (M9c) containing sodium phosphate heptahydrate, dibasic (6.8 g/liter), potassium phosphate, monobasic (3 g/liter), sodium chloride (0.5 g/liter), 2% glucose, ammonium chloride (1 g/liter), calcium chloride (0.1 mM), magnesium sulfate (2 mM), ferric citrate (500 μM),

p-aminobenzoic acid (2 mg/liter), inositol (20 mg/liter), adenine (5 mg/liter), uracil (20 mg/liter), tryptophan (40 mg/liter), tyrosine (1.2 mg/liter), and the remaining 18 amino acids (80 mg/liter each). Starter cultures grown to stationary phase were then diluted 1:100 into a selective modified M9 medium (M9sa), which is identical to M9c but lacks cysteine and methionine. Cultures were inoculated in sterile Nunc Edge 2.0 96-well plates with side reservoirs filled with 1 ml of water. The edges between plate tops and bottoms were sealed with parafilm. Cells were grown in a Spark plate reader (Tecan) at 37 °C, with shaking (90 rpm), at an amplitude of 3 mm in double-orbital mode. Optical density (OD) was measured at 600 nm every 5 min for 48 h. For end point measurements, all conditions were the same except that cells were grown in incubators at the indicated temperature, with shaking at 250 rpm, for 48 h.

Fluorescence measurements

To evaluate the cellular expression of Fds, the genes encoding each Fd were expressed as fusions to a monomeric RFP with a 12-amino acid linker (105). Each vector was transformed into *E. coli* EW11 cells, alongside a plasmid (pSAC01) constitutively expressing SIR and FNR (53). Transformed cells were grown under conditions identical to those described for the cellular assay, with the exception of being grown in M9c at all steps. After 24 h, end point OD and RFP fluorescence ($\lambda_{excitation}$ = 560 nm; $\lambda_{emission}$ = 650 nm) were measured.

Statistics

Error bars represent S.D. calculated from three or more biological replicates. Independent two-tailed *t* tests were applied to compare differences between all relevant samples ($\alpha = 0.05$).

Data availability

The structure presented in this study is available in the PDB with code 6VJV. All remaining data are contained within this article.

Author contributions—I. J. C., J. T. A., G. N. B., and J. J. S. conceptualization; I. J. C. data curation; I. J. C. and J. L. O. formal analysis; I. J. C., J. L. O., W. X., D. K., J. T. A., O. N. S., M. D. M., and G. N. P. investigation; I. J. C. and J. L. O. visualization; I. J. C., J. L. O., D. K., J. T. A., O. N. S., M. D. M., G. N. P., and J. J. S. methodology; I. J. C., J. L. O., and J. J. S. writing-original draft; I. J. C., J. L. O., W. X., D. K., J. T. A., O. N. S., M. D. M., G. N. P., G. N. B., and J. J. S. writing-review and editing; G. N. P. and J. J. S. supervision; G. N. P. G. N. B., and J. J. S. funding acquisition.

Funding and additional information—This project was supported by DOE Grant DE-SC0014462 (to G. N. B. and J. J. S.), NASA NAI Grant 80NSSC18M0093 (to G. N. B. and J. J. S.), NSF Grant 1231306 (to G. N. P.), and Moore Foundation Grant 7524 (to G. N. B. and J. J. S.). The GM/CA facility at the Advanced Proton Source has been funded in whole or in part with federal funds from the National Cancer Institute (Grant ACB-12002) and the National Institute of General Medical Sciences (Grant AGM-12006). The Eiger 16M detector at the GM/CA-XSD was funded by NIH Grant S10 OD012289. This research used resources of the Advanced Photon Source, a DOE Office of Science User Facility operated for the DOE Office of Science by the Argonne National Laboratory under Contract DE-AC02-06CH11357. I.J.C. and J.T.A. were supported by a Lodieska Stockbridge Vaughn Fellowship.

Conflict of interest—The authors declare that they have no conflicts of interest with the contents of this article.

Abbreviations—The abbreviations used are: ORF, open reading frame; aTc, anhydrotetracycline; ET, electron transfer; Fd, ferredoxin; FNR, ferredoxin-NADP reductase; IPTG, isopropyl β-d-1-thiogalactopyranoside; CAPS, *N*-cyclohexyl-3-aminopropanesulfonic acid; TAPS, *N*-[tris(hydroxymethyl)methyl]-3-aminopropanesulfonic acid; CHES, *N*-cyclohexyl-2-aminoethanesulfonic acid; ml-Fd1, *Mastigocladus laminosus* ferredoxin 1; NIR, nitrite reductase; nsp-Fd1, *Nostoc* sp. PCC 7119 ferredoxin 1; PcyA, phycocyanobilin:ferredoxin oxidoreductase; PebS, phycoerythrobilin synthase; pm9211-Fd1, *Prochlorococcus marinus* MIT9211 ferredoxin 1; pm9211-SIR, *Prochlorococcus marinus* MIT9211 sulfite reductase; pmN1-Fd1, *Prochlorococcus marinus* NATL1A ferredoxin 1; pmN2-Fd1, *Prochlorococcus marinus* NATL2A ferredoxin 1; pmN2-SIR *Prochlorococcus marinus* NATL2A sulfite reductase; PSI, photosystem I; PSII, photosystem II; pssm2-Fd, myovirus P-SSM2 ferredoxin; RFP, red fluorescent protein; s6803-Fd1, *Synechocystis* sp. PCC 6803 ferredoxin 1; SIR, sulfite reductase; SSN, sequence similarity network; te-Fd1, *Thermosynechococcus elongatus* ferredoxin 1; zm-Fd1, *Zea mays* ferredoxin 1; zm-FNR, *Zea mays* ferredoxin-NADP reductase; zm-SIR, *Zea mays* sulfite reductase.

References

1. Flombaum, P., Gallegos, J. L., Gordillo, R. A., Rincon, J., Zabala, L. L., Jiao, N., Karl, D. M., Li, W. K. W., Lomas, M. W., Veneziano, D., Vera, C. S., Vrugt, J. A., and Martiny, A. C. (2013) Present and future global distributions of the marine cyanobacteria *Prochlorococcus* and *Synechococcus*. *Proc. Natl. Acad. Sci. U.S.A.* **110,** 9824–9829 CrossRef Medline
2. Malmstrom, R. R., Coe, A., Kettler, G. C., Martiny, A. C., Frias-Lopez, J., Zinser, E. R., and Chisholm, S. W. (2010) Temporal dynamics of *Prochlorococcus* ecotypes in the Atlantic and Pacific oceans. *ISME J.* **4,** 1252–1264 CrossRef Medline
3. Martiny, A. C., Tai, A. P. K., Veneziano, D., Primeau, F., and Chisholm, S. W. (2009) Taxonomic resolution, ecotypes and the biogeography of *Prochlorococcus*. *Environ. Microbiol.* **11,** 823–832 CrossRef Medline
4. Zinser, E. R., Johnson, Z. I., Coe, A., Karaca, E., Veneziano, D., and Chisholm, S. W. (2007) Influence of light and temperature on *Prochlorococcus* ecotype distributions in the Atlantic Ocean. *Limnol. Oceanogr.* **52,** 2205–2220 CrossRef
5. Bertilsson, S., Berglund, O., Pullin, M., and Chisholm, S. (2005) Release of dissolved organic matter by *Prochlorococcus*. *Vie Milieu* **55,** 225–231
6. Dufresne, A., Garczarek, L., and Partensky, F. (2005) Accelerated evolution associated with genome reduction in a free-living prokaryote. *Genome Biol.* **6,** R14 CrossRef Medline
7. Kettler, G. C., Martiny, A. C., Huang, K., Zucker, J., Coleman, M. L., Rodrigue, S., Chen, F., Lapidus, A., Ferriera, S., Johnson, J., Steglich, C., Church, G. M., Richardson, P., and Chisholm, S. W. (2007) Patterns and implications of gene gain and loss in the evolution of *Prochlorococcus*. *PLoS Genet.* **3,** e231 CrossRef Medline
8. Rocap, G., Larimer, F. W., Lamerdin, J., Malfatti, S., Chain, P., Ahlgren, N. A., Arellano, A., Coleman, M., Hauser, L., Hess, W. R., Johnson, Z. I., Land, M., Lindell, D., Post, A. F., Regala, W., *et al.* (2003) Genome divergence in two *Prochlorococcus* ecotypes reflects oceanic niche differentiation. *Nature* **424,** 1042–1047 CrossRef Medline

9. Sun, Z., and Blanchard, J. L. (2014) Strong genome-wide selection early in the evolution of *Prochlorococcus* resulted in a reduced genome through the loss of a large number of small effect genes. *PLoS ONE* **9,** e88837 CrossRef Medline
10. Urbach, E., Scanlan, D. J., Distel, D. L., Waterbury, J. B., and Chisholm, S. W. (1998) Rapid diversification of marine picophytoplankton with dissimilar light-harvesting structures inferred from sequences of *Prochlorococcus* and *Synechococcus* (cyanobacteria). *J. Mol. Evol.* **46,** 188–201 CrossRef Medline
11. Chisholm, S. W., Frankel, S. L., Goericke, R., Olson, R. J., Palenik, B., Waterbury, J. B., West-Johnsrud, L., and Zettler, E. R. (1992) *Prochlorococcus marinus* nov. gen. nov. sp.: an oxyphototrophic marine prokaryote containing divinyl chlorophyll a and b. *Arch. Microbiol.* **157,** 297–300 CrossRef
12. Golden, S. S., Brusslan, J., and Haselkorn, R. (1986) Expression of a family of *psbA* genes encoding a photosystem II polypeptide in the cyanobacterium *Anacystis nidulans* R2. *EMBO J.* **5,** 2789–2798 CrossRef Medline
13. Berube, P. M., Rasmussen, A., Braakman, R., Stepanauskas, R., and Chisholm, S. W. (2019) Emergence of trait variability through the lens of nitrogen assimilation in *Prochlorococcus*. *eLife* **8,** e41043 CrossRef
14. Biller, S. J., Berube, P. M., Lindell, D., and Chisholm, S. W. (2015) *Prochlorococcus*: the structure and function of collective diversity. *Nat. Rev. Microbiol.* **13,** 13–27 CrossRef Medline
15. Sullivan, M. B., Coleman, M. L., Weigele, P., Rohwer, F., and Chisholm, S. W. (2005) Three *Prochlorococcus* cyanophage genomes: signature features and ecological interpretations. *PLoS Biol.* **3,** e144 CrossRef Medline
16. Labrie, S. J., Frois-Moniz, K., Osburne, M. S., Kelly, L., Roggensack, S. E., Sullivan, M. B., Gearin, G., Zeng, Q., Fitzgerald, M., Henn, M. R., and Chisholm, S. W. (2013) Genomes of marine cyanopodoviruses reveal multiple origins of diversity. *Environ. Microbiol.* **15,** 1356–1376 CrossRef Medline
17. Sieradzki, E. T., Ignacio-Espinoza, J. C., Needham, D. M., Fichot, E. B., and Fuhrman, J. A. (2019) Dynamic marine viral infections and major contribution to photosynthetic processes shown by spatiotemporal picoplankton metatranscriptomes. *Nat. Commun.* **10,** 1169 CrossRef Medline
18. Liu, R., Liu, Y., Chen, Y., Zhan, Y., and Zeng, Q. (2019) Cyanobacterial viruses exhibit diurnal rhythms during infection. *Proc. Natl. Acad. Sci. U.S.A.* **116,** 14077–14082 CrossRef Medline
19. Lindell, D., Jaffe, J. D., Coleman, M. L., Futschik, M. E., Axmann, I. M., Rector, T., Kettler, G., Sullivan, M. B., Steen, R., Hess, W. R., Church, G. M., and Chisholm, S. W. (2007) Genome-wide expression dynamics of a marine virus and host reveal features of co-evolution. *Nature* **449,** 83–86 CrossRef Medline
20. Puxty, R. J., Millard, A. D., Evans, D. J., and Scanlan, D. J. (2016) Viruses inhibit CO_2 fixation in the most abundant phototrophs on Earth. *Curr. Biol.* **26,** 1585–1589 CrossRef Medline
21. Puxty, R. J., Evans, D. J., Millard, A. D., and Scanlan, D. J. (2018) Energy limitation of cyanophage development: implications for marine carbon cycling. *ISME J.* **12,** 1273–1286 CrossRef Medline
22. Lindell, D., Sullivan, M. B., Johnson, Z. I., Tolonen, A. C., Rohwer, F., and Chisholm, S. W. (2004) Transfer of photosynthesis genes to and from *Prochlorococcus* viruses. *Proc. Natl. Acad. Sci. U.S.A.* **101,** 11013–11018 CrossRef Medline
23. Clokie, M. R. J., Shan, J., Bailey, S., Jia, Y., Krisch, H. M., West, S., and Mann, N. H. (2006) Transcription of a "photosynthetic" T4-type phage during infection of a marine cyanobacterium. *Environ. Microbiol.* **8,** 827–835 CrossRef Medline
24. Sharon, I., Tzahor, S., Williamson, S., Shmoish, M., Man-Aharonovich, D., Rusch, D. B., Yooseph, S., Zeidner, G., Golden, S. S., Mackey, S. R., Adir, N., Weingart, U., Horn, D., Venter, J. C., Mandel-Gutfreund, Y., *et al.* (2007) Viral photosynthetic reaction center genes and transcripts in the marine environment. *ISME J.* **1,** 492–501 CrossRef Medline
25. Sharon, I., Alperovitch, A., Rohwer, F., Haynes, M., Glaser, F., Atamna-Ismaeel, N., Pinter, R. Y., Partensky, F., Koonin, E. V., Wolf, Y. I., Nelson, N., and Béjà, O. (2009) Photosystem I gene cassettes are present in marine virus genomes. *Nature* **461,** 258–262 CrossRef Medline
26. Puxty, R. J., Millard, A. D., Evans, D. J., and Scanlan, D. J. (2015) Shedding new light on viral photosynthesis. *Photosynth. Res.* **126,** 71–97 CrossRef Medline
27. Dammeyer, T., Bagby, S. C., Sullivan, M. B., Chisholm, S. W., and Frankenberg-Dinkel, N. (2008) Efficient phage-mediated pigment biosynthesis in oceanic cyanobacteria. *Curr. Biol.* **18,** 442–448 CrossRef Medline
28. Ledermann, B., Schwan, M., Sommerkamp, J. A., Hofmann, E., Béjà, O., and Frankenberg-Dinkel, N. (2018) Evolution and molecular mechanism of four-electron reducing ferredoxin-dependent bilin reductases from oceanic phages. *FEBS J.* **285,** 339–356 CrossRef Medline
29. Atkinson, J. T., Campbell, I., Bennett, G. N., and Silberg, J. J. (2016) Cellular assays for ferredoxins: a strategy for understanding electron flow through protein carriers that link metabolic pathways. *Biochemistry* **55,** 7047–7064 CrossRef Medline
30. Burkhart, B. W., Febvre, H. P., and Santangelo, T. J. (2019) Distinct physiological roles of the three ferredoxins encoded in the hyperthermophilic archaeon *Thermococcus kodakarensis*. *mBio* **10,** e02807-18 CrossRef
31. Cassier-Chauvat, C., and Chauvat, F. (2014) Function and regulation of ferredoxins in the cyanobacterium, *Synechocystis* PCC6803: recent advances. *Life* **4,** 666–680 CrossRef Medline
32. Terauchi, A. M., Lu, S., Zaffagnini, M., Tappa, S., Hirasawa, M., Tripathy, J. N., Knaff, D. B., Farmer, P. J., Lemaire, D., Hase, T., and Merchant, S. S. (2009) Pattern of expression and substrate specificity of chloroplast ferredoxins from *Chlamydomonas reinhardtii*. *J. Biol. Chem.* **284,** 25867–25878 CrossRef Medline
33. Onda, Y., Matsumura, T., Kimata-Ariga, Y., Sakakibara, H., Sugiyama, T., and Hase, T. (2000) Differential interaction of maize root ferredoxin: $NADP^+$ oxidoreductase with photosynthetic and non-photosynthetic ferredoxin isoproteins. *Plant Physiol.* **123,** 1037–1045 CrossRef Medline
34. Finn, R. D., Attwood, T. K., Babbitt, P. C., Bateman, A., Bork, P., Bridge, A. J., Chang, H.-Y., Dosztányi, Z., El-Gebali, S., Fraser, M., Gough, J., Haft, D., Holliday, G. L., Huang, H., Huang, X., *et al.* (2017) InterPro in 2017: beyond protein family and domain annotations. *Nucleic Acids Res.* **45,** D190–D199 CrossRef Medline
35. Cornelissen, A., Hardies, S. C., Shaburova, O. V., Krylov, V. N., Mattheus, W., Kropinski, A. M., and Lavigne, R. (2012) Complete genome sequence of the giant virus OBP and comparative genome analysis of the diverse KZ-related phages. *J. Virol.* **86,** 1844–1852 CrossRef Medline
36. Gerlt, J. A. (2017) Genomic enzymology: web tools for leveraging protein family sequence–function space and genome context to discover novel functions. *Biochemistry* **56,** 4293–4308 CrossRef Medline
37. Campbell, I. J., Bennett, G. N., and Silberg, J. J. (2019) Evolutionary relationships between low potential ferredoxin and flavodoxin electron carriers. *Front. Energy Res.* **7,** 79 CrossRef
38. Kim, J. Y., Nakayama, M., Toyota, H., Kurisu, G., and Hase, T. (2016) Structural and mutational studies of an electron transfer complex of maize sulfite reductase and ferredoxin. *J. Biochem. (Tokyo)* **160,** 101–109 CrossRef Medline
39. Kurisu, G., Kusunoki, M., Katoh, E., Yamazaki, T., Teshima, K., Onda, Y., Kimata-Ariga, Y., and Hase, T. (2001) Structure of the electron transfer complex between ferredoxin and ferredoxin-$NADP^+$ reductase. *Nat. Struct. Biol.* **8,** 117–121 CrossRef Medline
40. Atkinson, H. J., Morris, J. H., Ferrin, T. E., and Babbitt, P. C. (2009) Using sequence similarity networks for visualization of relationships across diverse protein superfamilies. *PLoS ONE* **4,** e4345 CrossRef Medline
41. van den Heuvel, R. H. H., Svergun, D. I., Petoukhov, M. V., Coda, A., Curti, B., Ravasio, S., Vanoni, M. A., and Mattevi, A. (2003) The active conformation of glutamate synthase and its binding to ferredoxin. *J. Mol. Biol.* **330,** 113–128 CrossRef Medline
42. Lelong, C., Boekema, E. J., Kruip, J., Bottin, H., Rögner, M., and Sétif, P. (1996) Characterization of a redox active cross-linked complex between cyanobacterial photosystem I and soluble ferredoxin. *EMBO J.* **15,** 2160–2168 CrossRef
43. Palma, P. N., Lagoutte, B., Krippahl, L., Moura, J. J. G., and Guerlesquin, F. (2005) *Synechocystis* ferredoxin/ferredoxin-$NADP^+$-reductase/$NADP^+$ complex: structural model obtained by NMR-restrained docking. *FEBS Lett.* **579,** 4585–4590 CrossRef Medline

44. Morales, R., Kachalova, G., Vellieux, F., Charon, M.-H., and Frey, M. (2000) Crystallographic studies of the interaction between the ferredoxin-NADP$^+$ reductase and ferredoxin from the cyanobacterium *Anabaena*: looking for the elusive ferredoxin molecule. *Acta Crystallogr. D Biol. Crystallogr.* **56,** 1408–1412 CrossRef Medline
45. Kubota-Kawai, H., Mutoh, R., Shinmura, K., Sétif, P., Nowaczyk, M. M., Rögner, M., Ikegami, T., Tanaka, H., and Kurisu, G. (2018) X-ray structure of an asymmetrical trimeric ferredoxin-photosystem I complex. *Nat. Plants* **4,** 218–224 CrossRef Medline
46. Okada, K. (2009) HO1 and PcyA proteins involved in phycobilin biosynthesis form a 1:2 complex with ferredoxin-1 required for photosynthesis. *FEBS Lett.* **583,** 1251–1256 CrossRef Medline
47. Okada, K., and Hase, T. (2005) Cyanobacterial non-mevalonate pathway: (*E*)-4-hydroxy-3-methylbut-2-enyl diphosphate synthase interacts with ferredoxin in *Thermosynechococcus elongatus* BP-1. *J. Biol. Chem.* **280,** 20672–20679 CrossRef Medline
48. Motomura, T., Zuccarello, L., Sétif, P., Boussac, A., Umena, Y., Lemaire, D., Tripathy, J. N., Sugiura, M., Hienerwadel, R., Shen, J.-R., and Berthomieu, C. (2019) An alternative plant-like cyanobacterial ferredoxin with unprecedented structural and functional properties. *Biochim. Biophys. Acta Bioenerg.* **1860,** 148084 CrossRef Medline
49. Hirasawa, M., Nakayama, M., Hase, T., and Knaff, D. B. (2004) Oxidation-reduction properties of maize ferredoxin:sulfite oxidoreductase. *Biochim. Biophys. Acta Bioenerg.* **1608,** 140–148 CrossRef Medline
50. Swamy, U., Wang, M., Tripathy, J. N., Kim, S.-K., Hirasawa, M., Knaff, D. B., and Allen, J. P. (2005) Structure of spinach nitrite reductase: implications for multi-electron reactions by the iron−sulfur:siroheme cofactor. *Biochemistry* **44,** 16054–16063 CrossRef Medline
51. Sullivan, M. B., Waterbury, J. B., and Chisholm, S. W. (2003) Cyanophages infecting the oceanic cyanobacterium *Prochlorococcus*. *Nature* **424,** 1047–1051 CrossRef
52. Altschul, S. F., Gish, W., Miller, W., Myers, E. W., and Lipman, D. J. (1990) Basic local alignment search tool. *J. Mol. Biol.* **215,** 403–410 CrossRef Medline
53. Atkinson, J. T., Campbell, I. J., Thomas, E. E., Bonitatibus, S. C., Elliott, S. J., Bennett, G. N., and Silberg, J. J. (2019) Metalloprotein switches that display chemical-dependent electron transfer in cells. *Nat. Chem. Biol.* **15,** 189–195 CrossRef Medline
54. Stephens, P. J., Thomson, A. J., Dunn, J. B. R., Keiderling, T. A., Rawlings, J., Rao, K. K., and Hall, D. O. (1978) Circular dichroism and magnetic circular dichroism of iron-sulfur proteins. *Biochemistry* **17,** 4770–4778 CrossRef Medline
55. Ta, D. T., and Vickery, L. E. (1992) Cloning, sequencing, and overexpression of a [2Fe-2S] ferredoxin gene from *Escherichia coli*. *J. Biol. Chem.* **267,** 11120–11125
56. Jung, Y.-S., Gao-Sheridan, H. S., Christiansen, J., Dean, D. R., and Burgess, B. K. (1999) Purification and biophysical characterization of a new [2Fe-2S] ferredoxin from *Azotobacter vinelandii,* a putative [Fe-S] cluster assembly/repair protein. *J. Biol. Chem.* **274,** 32402–32410 CrossRef Medline
57. Leal, S. S., and Gomes, C. M. (2008) On the relative contribution of ionic interactions over iron–sulfur clusters to ferredoxin stability. *Biochim. Biophys. Acta Proteins Proteomics* **1784,** 1596–1600 CrossRef Medline
58. Lei, H., Guo, Y., Hu, X., Hu, C., Hu, X., and Li, H. (2017) Reversible unfolding and folding of the metalloprotein ferredoxin revealed by single-molecule atomic force microscopy. *J. Am. Chem. Soc.* **139,** 1538–1544 CrossRef Medline
59. Higgins, C. L., Meyer, J., and Wittung-Stafshede, P. (2002) Exceptional stability of a [2Fe–2S] ferredoxin from hyperthermophilic bacterium *Aquifex aeolicus*. *Biochim. Biophys. Acta Proteins Proteomics* **1599,** 82–89 CrossRef
60. Pereira, M. M., Jones, K. L., Campos, M. G., Melo, A. M. P., Saraiva, L. M., Louro, R. O., Wittung-Stafshede, P., and Teixeira, M. (2002) A ferredoxin from the thermohalophilic bacterium *Rhodothermus marinus*. *Biochim. Biophys. Acta Proteins Proteomics* **1601,** 1–8 CrossRef Medline
61. Moczygemba, C., Guidry, J., Jones, K. L., Gomes, C. M., Teixeira, M., and Wittung-Stafshede, P. (2001) High stability of a ferredoxin from the hyperthermophilic archaeon *A. ambivalens*: involvement of electrostatic interactions and cofactors. *Protein Sci.* **10,** 1539–1548 CrossRef Medline
62. Osteryoung, J. G., and Osteryoung, R. A. (1985) Square wave voltammetry. *Anal. Chem.* **57,** 101–110 CrossRef
63. Jin, S., Kurtz, D. M., Liu, Z.-J., Rose, J., and Wang, B.-C. (2004) Displacement of iron by zinc at the diiron site of *Desulfovibrio vulgaris* rubrerythrin: X-ray crystal structure and anomalous scattering analysis. *J. Inorg. Biochem.* **98,** 786–796 CrossRef Medline
64. Iametti, S., Uhlmann, H., Sala, N., Bernhardt, R., Ragg, E., and Bonomi, F. (1996) Reversible, non-denaturing metal substitution in bovine adrenodoxin and spinach ferredoxin and the different reactivities of [2Fe-2S]-cluster-containing proteins. *Eur. J. Biochem.* **239,** 818–826 CrossRef Medline
65. Kojoh, K., Matsuzawa, H., and Wakagi, T. (1999) Zinc and an N-terminal extra stretch of the ferredoxin from a thermoacidophilic archaeon stabilize the molecule at high temperature. *Eur. J. Biochem.* **264,** 85–91 CrossRef Medline
66. Sazinsky, M. H., LeMoine, B., Orofino, M., Davydov, R., Bencze, K. Z., Stemmler, T. L., Hoffman, B. M., Argüello, J. M., and Rosenzweig, A. C. (2007) Characterization and structure of a Zn^{2+} and [2Fe-2S]-containing copper chaperone from *Archaeoglobus fulgidus*. *J. Biol. Chem.* **282,** 25950–25959 CrossRef Medline
67. Lo Conte, L., Ailey, B., Hubbard, T. J., Brenner, S. E., Murzin, A. G., and Chothia, C. (2000) SCOP: a Structural Classification of Proteins database. *Nucleic Acids Res.* **28,** 257–259 CrossRef Medline
68. Fish, A., Danieli, T., Ohad, I., Nechushtai, R., and Livnah, O. (2005) Structural basis for the thermostability of ferredoxin from the cyanobacterium *Mastigocladus laminosus*. *J. Mol. Biol.* **350,** 599–608 CrossRef Medline
69. Morales, R., Charon, M. H., Hudry-Clergeon, G., Pétillot, Y., Norager, S., Medina, M., and Frey, M. (1999) Refined X-ray structures of the oxidized, at 1.3 Å, and reduced, at 1.17 Å, [2Fe-2S] ferredoxin from the cyanobacterium *Anabaena* PCC7119 show redox-linked conformational changes. *Biochemistry* **38,** 15764–15773 CrossRef Medline
70. Mutoh, R., Muraki, N., Shinmura, K., Kubota-Kawai, H., Lee, Y.-H., Nowaczyk, M. M., Rögner, M., Hase, T., Ikegami, T., and Kurisu, G. (2015) X-ray structure and nuclear magnetic resonance analysis of the interaction sites of the Ga-substituted cyanobacterial ferredoxin. *Biochemistry* **54,** 6052–6061 CrossRef Medline
71. Sakakibara, Y., Kimura, H., Iwamura, A., Saitoh, T., Ikegami, T., Kurisu, G., and Hase, T. (2012) A new structural insight into differential interaction of cyanobacterial and plant ferredoxins with nitrite reductase as revealed by NMR and X-ray crystallographic studies. *J. Biochem. (Tokyo)* **151,** 483–492 CrossRef Medline
72. Ashkenazy, H., Abadi, S., Martz, E., Chay, O., Mayrose, I., Pupko, T., and Ben-Tal, N. (2016) ConSurf 2016: an improved methodology to estimate and visualize evolutionary conservation in macromolecules. *Nucleic Acids Res.* **44,** W344–W350 CrossRef Medline
73. Barstow, B., Agapakis, C. M., Boyle, P. M., Grandl, G., Silver, P. A., and Wintermute, E. H. (2011) A synthetic system links FeFe-hydrogenases to essential *E. coli* sulfur metabolism. *J. Biol. Eng.* **5,** 7 CrossRef Medline
74. Houot, L., Floutier, M., Marteyn, B., Michaut, M., Picciocchi, A., Legrain, P., Aude, J.-C., Cassier-Chauvat, C., and Chauvat, F. (2007) Cadmium triggers an integrated reprogramming of the metabolism of *Synechocystis* PCC6803, under the control of the Slr1738 regulator. *BMC Genomics* **8,** 350 CrossRef Medline
75. Kimata, Y., and Hase, T. (1989) Localization of ferredoxin isoproteins in mesophyll and bundle sheath cells in maize leaf. *Plant Physiol.* **89,** 1193–1197 CrossRef Medline
76. Singh, A. K., Elvitigala, T., Cameron, J. C., Ghosh, B. K., Bhattacharyya-Pakrasi, M., and Pakrasi, H. B. (2010) Integrative analysis of large scale expression profiles reveals core transcriptional response and coordination between multiple cellular processes in a cyanobacterium. *BMC Syst. Biol.* **4,** 105 CrossRef
77. Pochapsky, T. C., Jain, N. U., Kuti, M., Lyons, T. A., and Heymont, J. (1999) A refined model for the solution structure of oxidized putidaredoxin. *Biochemistry* **38,** 4681–4690 CrossRef Medline

78. Bottin, H., and Lagoutte, B. (1992) Ferrodoxin and flavodoxin from the cyanobacterium *Synechocystis* sp. PCC 6803. *Biochim. Biophys. Acta Bioenerg.* **1101,** 48–56 CrossRef
79. Hurley, J. K., Weber-Main, A. M., Hodges, A. E., Stankovich, M. T., Benning, M. M., Holden, H. M., Cheng, H., Xia, B., Markley, J. L., Genzor, C., Gomez-Moreno, C., Hafezi, R., and Tollin, G. (1997) Iron-sulfur cluster cysteine-to-serine mutants of *Anabaena* -2Fe-2S- ferredoxin exhibit unexpected redox properties and are competent in electron transfer to ferredoxin:$NADP^+$ reductase. *Biochemistry* **36,** 15109–15117 CrossRef Medline
80. Nechushtai, R., Lammert, H., Michaeli, D., Eisenberg-Domovich, Y., Zuris, J. A., Luca, M. A., Capraro, D. T., Fish, A., Shimshon, O., Roy, M., Schug, A., Whitford, P. C., Livnah, O., Onuchic, J. N., and Jennings, P. A. (2011) Allostery in the ferredoxin protein motif does not involve a conformational switch. *Proc. Natl. Acad. Sci. U.S.A.* **108,** 2240–2245 CrossRef Medline
81. Chang, C.-J., Lee, C.-C., Chan, Y.-T., Trudeau, D. L., Wu, M.-H., Tsai, C.-H., Yu, S.-M., Ho, T.-H. D., Wang, A. H.-J., Hsiao, C.-D., Arnold, F. H., and Chao, Y.-C. (2016) Exploring the mechanism responsible for cellulase thermostability by structure-guided recombination. *PLoS ONE* **11,** e0147485 CrossRef Medline
82. Otey, C. R., Landwehr, M., Endelman, J. B., Hiraga, K., Bloom, J. D., and Arnold, F. H. (2006) Structure-guided recombination creates an artificial family of cytochromes P450. *PLoS Biol.* **4,** e112 CrossRef Medline
83. Andreae, M. O. (1990) Ocean-atmosphere interactions in the global biogeochemical sulfur cycle. *Mar. Chem.* **30,** 1–29 CrossRef
84. Kiene, R. P., Linn, L. J., González, J., Moran, M. A., and Bruton, J. A. (1999) Dimethylsulfoniopropionate and methanethiol are important precursors of methionine and protein-sulfur in marine bacterioplankton. *Appl. Environ. Microbiol.* **65,** 4549–4558 CrossRef Medline
85. del Valle, D., Martínez-García, S., Sañudo-Wilhelmy, S., Kiene, R., and Karl, D. (2015) Methionine and dimethylsulfoniopropionate as sources of sulfur to the microbial community of the North Pacific Subtropical Gyre. *Aquat. Microb. Ecol.* **75,** 103–116 CrossRef
86. Mutter, A. C., Tyryshkin, A. M., Campbell, I. J., Poudel, S., Bennett, G. N., Silberg, J. J., Nanda, V., and Falkowski, P. G. (2019) De novo design of symmetric ferredoxins that shuttle electrons *in vivo*. *Proc. Natl. Acad. Sci. U.S.A.* **116,** 14557–14562 CrossRef Medline
87. Wu, B., Atkinson, J. T., Kahanda, D., Bennett, G. N., and Silberg, J. J. (2020) Combinatorial design of chemical-dependent protein switches for controlling intracellular electron transfer. *AIChE J.* **66,** e16796 CrossRef
88. Engler, C., Kandzia, R., and Marillonnet, S. (2008) A one pot, one step, precision cloning method with high throughput capability. *PLoS ONE* **3,** e3647 CrossRef Medline
89. Salis, H. M. (2011) The ribosome binding site calculator. *Methods Enzymol.* **498,** 19–42 CrossRef
90. Shannon, P., Markiel, A., Ozier, O., Baliga, N. S., Wang, J. T., Ramage, D., Amin, N., Schwikowski, B., and Ideker, T. (2003) Cytoscape: a software environment for integrated models of biomolecular interaction networks. *Genome Res.* **13,** 2498–2504 CrossRef Medline
91. Edgar, R. C. (2004) MUSCLE : multiple sequence alignment with high accuracy and high throughput. *Nucleic Acids Res.* **32,** 1792–1797 CrossRef Medline
92. Li, B., and Elliott, S. J. (2016) The catalytic bias of 2-oxoacid:ferredoxin oxidoreductase in CO_2: evolution and reduction through a ferredoxin-mediated electrocatalytic assay. *Electrochim. Acta* **199,** 349–356 CrossRef
93. Vonrhein, C., Flensburg, C., Keller, P., Sharff, A., Smart, O., Paciorek, W., Womack, T., and Bricogne, G. (2011) Data processing and analysis with the *autoPROC* toolbox. *Acta Crystallogr. D Biol. Crystallogr.* **67,** 293–302 CrossRef Medline
94. Kabsch, W. (2010) XDS. *Acta Crystallogr. D Biol. Crystallogr.* **66,** 125–132 CrossRef Medline
95. Evans, P. R., and Murshudov, G. N. (2013) How good are my data and what is the resolution? *Acta Crystallogr. D Biol. Crystallogr.* **69,** 1204–1214 CrossRef Medline
96. Shinohara, F., Kurisu, G., Hanke, G., Bowsher, C., Hase, T., and Kimata-Ariga, Y. (2017) Structural basis for the isotype-specific interactions of ferredoxin and ferredoxin: $NADP^+$ oxidoreductase: an evolutionary switch between photosynthetic and heterotrophic assimilation. *Photosynth. Res.* **134,** 281–289 CrossRef Medline
97. Emsley, P., and Cowtan, K. (2004) *Coot*: model-building tools for molecular graphics. *Acta Crystallogr. D Biol. Crystallogr.* **60,** 2126–2132 CrossRef Medline
98. Afonine, P. V., Grosse-Kunstleve, R. W., Echols, N., Headd, J. J., Moriarty, N. W., Mustyakimov, M., Terwilliger, T. C., Urzhumtsev, A., Zwart, P. H., and Adams, P. D. (2012) Towards automated crystallographic structure refinement with *phenix.refine*. *Acta Crystallogr. D Biol. Crystallogr.* **68,** 352–367 CrossRef Medline
99. Yennamalli, R., Arangarasan, R., Bryden, A., Gleicher, M., and Phillips, G. N. (2014) Using a commodity high-definition television for collaborative structural biology. *J. Appl. Crystallogr.* **47,** 1153–1157 CrossRef Medline
100. Thorn, A., and Sheldrick, G. M. (2011) *ANODE*: anomalous and heavy-atom density calculation. *J. Appl. Crystallogr.* **44,** 1285–1287 CrossRef Medline
101. Morin, A., Eisenbraun, B., Key, J., Sanschagrin, P. C., Timony, M. A., Ottaviano, M., and Sliz, P. (2013) Collaboration gets the most out of software. *eLife* **2,** e01456 CrossRef Medline
102. Berman, H., Henrick, K., and Nakamura, H. (2003) Announcing the worldwide Protein Data Bank. *Nat. Struct. Mol. Biol.* **10,** 980 CrossRef Medline
103. Xu, D., Jaroszewski, L., Li, Z., and Godzik, A. (2014) FFAS-3D: improving fold recognition by including optimized structural features and template re-ranking. *Bioinformatics* **30,** 660–667 CrossRef Medline
104. Canutescu, A. A., Shelenkov, A. A., and Dunbrack, R. L. (2003) A graph-theory algorithm for rapid protein side-chain prediction. *Protein Sci.* **12,** 2001–2014 CrossRef
105. Campbell, R. E., Tour, O., Palmer, A. E., Steinbach, P. A., Baird, G. S., Zacharias, D. A., and Tsien, R. Y. (2002) A monomeric red fluorescent protein. *Proc. Natl. Acad. Sci. U.S.A.* **99,** 7877–7882 CrossRef Medline